Charge Transfer and Built-in Electric Fields between a Crystalline Oxide and Silicon

Z. H. Lim,[1] N. F. Quackenbush,[2] A. N. Penn,[3] M. Chrysler,[1] M. Bowden,[4] Z. Zhu,[4] J. M. Ablett,[5] T.-L. Lee,[6] J. M. LeBeau,[3] J. C. Woicik,[2] P. V. Sushko,[7] S. A. Chambers,[7] and J. H. Ngai[1]

[1]*Department of Physics, University of Texas-Arlington, Arlington, Texas 76019, USA*
[2]*Material Measurement Laboratory, Materials Measurement Science Division, National Institute of Standards and Technology, Gaithersburg, Maryland 20899, USA*
[3]*Department of Materials Science and Engineering, North Carolina State University, Raleigh, North Carolina 27695, USA*
[4]*Environmental Molecular Sciences Laboratory Pacific Northwest National Laboratory, Richland, Washington 99352, USA*
[5]*Synchrotron SOLEIL, L'Orme des Merisiers, Saint-Aubin, BP 48, 91192 Gif-sur-Yvette, France*
[6]*Diamond Light Source, Ltd., Harwell Science and Innovation Campus, Didcot, Oxfordshire OX11 0DE, United Kingdom*
[7]*Physical and Computational Sciences Directorate, Pacific Northwest National Laboratory, Richland, Washington 99352, USA*

(Received 18 October 2018; revised manuscript received 16 January 2019; published 11 July 2019; corrected 17 July 2019)

We report charge transfer and built-in electric fields across the epitaxial $SrNb_xTi_{1-x}O_{3-\delta}/Si(001)$ interface. Electrical transport measurements indicate the formation of a hole gas in the Si and the presence of built-in fields. Hard x-ray photoelectron measurements reveal pronounced asymmetries in core-level spectra that arise from these built-in fields. Theoretical analysis of core-level spectra enables built-in fields and the resulting band bending to be spatially mapped across the heterojunction. The demonstration of tunable charge transfer, built-in fields, and the spatial mapping of the latter, lays the groundwork for the development of electrically coupled, functional heterojunctions.

DOI: 10.1103/PhysRevLett.123.026805

Charge transfer across semiconductor heterojunctions and the electric fields that arise therefrom underpin the functionality of virtually all semiconductor devices, such as transistors, solar cells, light emitting diodes, and semiconductor-based lasers. The *p-n* junction is the most ubiquitous building block for such devices [1]. Other examples include isotype (e.g., *n-n*) and doped-intrinsic heterojunctions, the latter of which have led to fundamental discoveries, such as the fractional quantum Hall effect [2]. Charge transfer across heterojunctions has thus had broad and immense impact.

Advancements in epitaxial growth now enable charge transfer to be explored across heterojunctions between crystalline oxides and semiconductors [3]. The resulting atomically abrupt interfaces enable continuity in the electric displacement [4–7], which is essential for charge transfer and the formation of built-in fields. The short electronic length scales, highly tunable carrier densities, sizable band offsets, and large temperature-dependent dielectric constants of oxides can give rise to novel electrical behavior when interfaced with semiconductors. Such hybrid heterojunctions could be exploited in applications ranging from photocatalysis to nanophotonics [8–10]. Despite the ability to realize epitaxial semiconductor-oxide heterojunctions, tunable charge transfer and built-in fields have yet to be demonstrated or studied. Understanding charge transfer and built-in fields in semiconductor-oxide heterojunctions presents challenges, as the assumption of rigid band offsets under doping and other semiclassical approximations that largely describe conventional heterojunctions may have limited applicability. Given such challenges, the development of techniques to measure built-in fields and band alignments is also needed.

In this Letter, we demonstrate tunable charge transfer and built-in fields in a heterojunction comprised of Si and the archetype oxide semiconductor $SrTiO_3$ [11], in which the carrier density can be modulated via oxygen vacancies (δ) or Nb substitution (x), in $SrNb_xTi_{1-x}O_{3-\delta}$ (SNTO). As in heterojunctions of conventional semiconductors, charge transfer and built-in fields can be controlled by tuning carrier densities. We find that built-in fields and associated band bending can be induced to form a hole gas in the Si near room temperature. Hard x-ray photoelectron spectroscopy (HAXPES) reveals pronounced asymmetric features in core-level spectra for both SNTO and Si [12]. We show that analysis of the asymmetries enables built-in fields and band alignment to be spatially mapped across the interface. The demonstration of tunable charge transfer, built-in fields, and mapping of the latter via HAXPES lays the groundwork for the development of functional semiconductor-oxide heterojunctions that are coupled through charge transfer.

Epitaxial 12-nm-thick SNTO films were grown by oxide MBE on undoped Czochralski-grown Si (001) (see Supplemental Material [13]). These films are relaxed with respect to Si for all x, and the lattice parameters increase with x, as shown in Fig. S1. The interface between the SNTO and Si is atomically abrupt, as shown in the high-angle annular dark-field (HAADF) scanning transmission

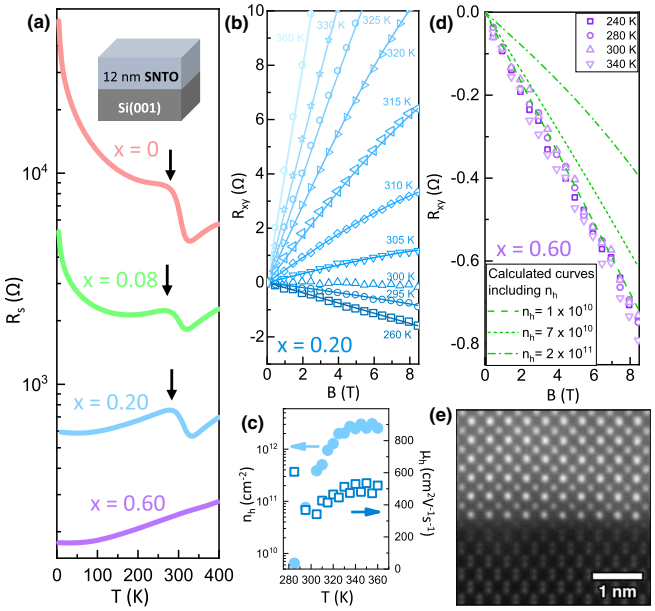

FIG. 1. (a) R_s for various x, showing anomalies (arrows) in the $x = 0$, 0.084, and 0.20 heterojunctions. (b) R_{xy} for the $x = 0.20$ heterojunction, which exhibits a crossover in sign of the slope. Data are shown as symbols, while calculated fits to the data are shown as lines. (c) n_h and μ_h of holes determined from fits of the R_{xy} data for the $x = 0.20$ heterojunction. (d) R_{xy} for the $x = 0.60$ heterojunction. (e) HAADF-STEM image of the $x = 0.20$ heterojunction, showing an atomically abrupt interface.

electron microscopy (STEM) image of the $x = 0.20$ heterojunction (Fig. 1(e) and Fig. S2).

Signatures of hole gas formation in Si are found in the sheet (R_s) and Hall (R_{xy}) resistances. Figure 1(a) shows R_s for the $x = 0$, 0.084, 0.20, and 0.60 heterojunctions. At low temperatures, R_s exhibits insulating behavior (i.e., $dR_s/dT < 0$) for $x = 0$ and progresses to metallic behavior ($dR_s/dT > 0$) as x increases to 0.60. At high temperatures, nonmonotonic anomalies are observed from $T \sim 265$ to ~ 280 K (arrows) for the $x = 0$, 0.084, and 0.20 heterojunctions, above which a sharp drop in R_s is observed, followed by metallic behavior. The anomalies in R_s are accompanied by nonlinear behavior and a crossover in the slope of R_{xy} from negative to positive with increasing temperature, as shown by the symbols in Fig. 1(b) [Figs. S3(a) and S3(b)] for the $x = 0.20$ ($x = 0$, 0.084) heterojunction(s).

The nonlinear behavior and crossover in sign of R_{xy} are consistent with the emergence of a hole gas in Si near the interface. To quantify the sheet density and mobility of the hole gas, we analyze the R_{xy} data using a two-carrier model that is parametrized by the sheet carrier densities n_h, n_e and mobilities μ_h, μ_e of the hole and electron carriers in Si and SNTO, respectively (see Supplemental Material [13]) [20]. The fits to the R_{xy} data for the $x = 0.20$ ($x = 0$, 0.084) heterojunction(s) are shown as lines in Fig. 1(b) (Supplemental Material Figs. S3(a) and S3(b)]. The values of n_h and μ_h derived from those fits for the $x = 0.20$ ($x = 0$, 0.084) heterojunction(s) are shown in Fig. 1(c) (Supplemental Material Figs. S3(c) and S3(d)]. Hole sheet densities as high as $n_h \sim 3 \times 10^{12}$ cm^{-2} are observed for the $x = 0.20$ heterojunction at $T > 320$ K. Consistent with the bulk hole mobility of Si, an average μ_h of ~ 500 cm^2 V^{-1} s^{-1} is derived from the fits. In comparison, the corresponding values of n_e and μ_e from the SNTO layers do not vary appreciably over the temperature range $200 < T < 340$ K (Supplemental Material Table S1). Despite $n_h \ll n_e$, the conductivities of the electron and hole channels are comparable, since $\mu_h \gg \mu_e$ at ~ 300 K. We find that only the SNTO and the hole gas in the near-surface region of the Si contribute to the conductivity, as fits to the R_{xy} data indicate that conductivity in the bulk of the Si substrate is negligible (Supplemental Material Fig. S4). Neither the anomaly in R_s nor the crossover in the slope of R_{xy} are present in the $x = 0.60$ sample. An upper limit to n_h can be placed in the $x = 0.60$ heterojunction, as fits to the R_{xy} data indicate that $n_h > 2 \times 10^{10}$ cm^{-2} is not supported by the data, as shown in Fig. 1(d).

The emergence of a high-mobility hole gas indicates the presence of a built-in electric field across the SNTO/Si interface. We look for signatures of built-in fields using HAXPES with ~ 6 keV excitation, for which the probe depth exceeds the film thickness, enabling electronic information to be obtained across the buried interface [21]. Figures 2(a)–2(f) show core-level spectra for $x = 0$ and 0.20, along with reference spectra for bulk single crystals of $SrNb_{0.01}Ti_{0.99}O_3(001)$ and Si(001). The Nb $3d$ and Ti $2p$ spectra of the heterojunctions show multiple features indicating formal charges ranging down to zero. Angle-resolved HAXPES measurements (Supplemental Material Fig. S5) reveal that the lower valence spectral features are reduced in intensity relative to the dominant valence feature as the electron takeoff angle decreases. Similarly, these features are largely absent in measurements made at normal emission using a conventional x-ray photoemission spectroscopy (XPS) system (Supplemental Material Fig. S6), for which the probe depth is $\sim 3\times$ smaller than in HAXPES at $h\nu = 6$ keV. Thus, the lower valence features arise from Ti and Nb cations near the interface. We hypothesize that the lower valences arise from enhanced screening of Ti^{4+} and Nb^{5+} from itinerant electrons that have accumulated near the SNTO/Si interface due to a built-in field.

Evidence for built-in fields is also found in the unprecedented asymmetries seen in all heterojunction core-level spectra, as indicated by arrows in Figs. 2(a) and 2(c)–2(e). These asymmetries also exhibit a clear dependence on probe depth as they diminish, as the takeoff angle decreases in angle-resolved HAXPES measurements (Supplemental Material Fig. S5) and are absent in spectra measured using conventional XPS at normal emission (Supplemental Material Fig. S6). These dependences on probe depth

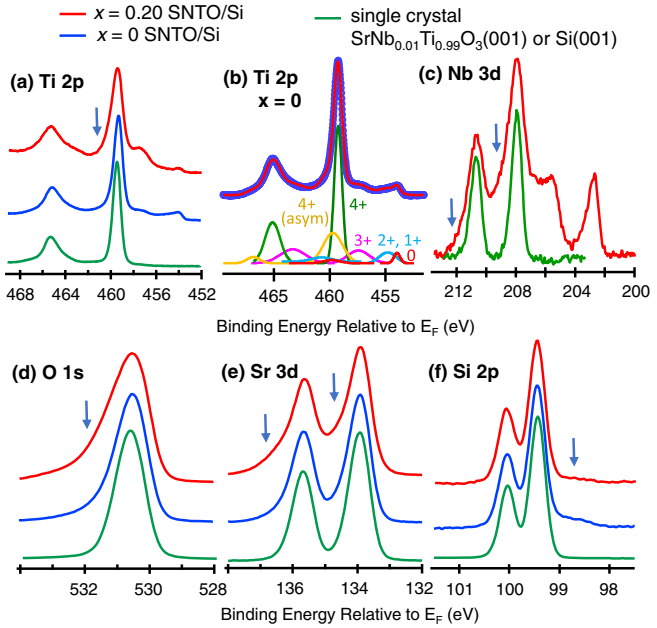

FIG. 2. (a)–(f) Ti $2p$, Nb $3d$, O $1s$, Sr $3d$, Si $2p$ spectra from SNTO/Si $x = 0.20$ (red) and $x = 0$ (blue) heterojunctions. Spectra from a 1 at.% Nb-doped STO(001) single crystal and Si(100) substrate are also shown (green) for comparison. The Ti $2p$ spectra exhibit oxidation states of $0 - 4+$ as shown by fits in (b). Also, note the asymmetric features observed in the core-level spectra from the heterojunctions (arrows) that are not present in the spectra of bulk substrates.

and the absence of asymmetry in the Ti $2p_{3/2}$ spectra of 12-nm-thick $x = 0$ and 0.10 films grown under identical conditions on LSAT(001) (Supplemental Material Fig. S7), or in bulk crystals of similar carrier concentration [22], indicate that the asymmetry is not due to shakeup [23]. For Si $2p$, an asymmetry to lower binding energy is observed [Fig. 2(f)], reminiscent of Ti silicide [24]. However, HAADF-STEM imaging does not show any interfacial Ti silicide whatsoever [Fig. 1(e) and Supplemental Material Fig. S2].

Capitalizing on the large probe depth of HAXPES near normal emission, we show that the asymmetric features in the SNTO and Si spectra are consistent with built-in fields and that spatial variations of these fields can be extracted from these data. To probe the connection between built-in electric fields and peak asymmetries, we model Si $2p$ and Ti $2p$ spectra for $x = 0$ and 0.20 (i.e., $SrNb_xTi_{1-x}O_{3-\delta}/Si$) using sums of spectra taken from pure, bulk crystals that are minimally affected by surface core-level shifts and band bending (Supplemental Material Fig. S8). To make the Ti $2p$ fitting tractable, we fit the heterojunction spectra and subtract all contributions due to valences other than $4+$ in the $2p_{3/2}$ branch and its asymmetry to higher binding energy [Fig. 2(b)]. The appropriate reference spectrum is assigned to each layer within the probe depth. All intensities are attenuated according to depth (z) using an inelastic damping factor of the form $\exp(-z/\lambda)$ in which λ is the attenuation length, estimated to be $\lambda \sim 7$ nm in Si and ~ 6 nm in $SrTiO_3$ [21]. A built-in electric field will shift the binding energies of all layers as illustrated schematically in Supplemental Material Fig. S9. The heterojunction spectra are then fit to sums of reference spectra over all layers by optimizing the layer-resolved binding energies.

The fitting starts by assigning randomly generated binding energies to all layers [21]. These energies are sorted and reassigned to the layers so the binding energy at maximum intensity, $\varepsilon_{\max}(j)$, is a monotonic function of depth. This peak binding energy set $\{\varepsilon_{\max}(j)\}$ is a measure of the band-edge profile because core-level binding energies, like valence band maxima (VBMs), scale linearly with electrostatic potential. The spectra were then summed to generate a trial simulated heterojunction spectrum $I_{\text{sim}}(\varepsilon)$. Optimization of the binding energies ε proceeds so as to minimize a cost function, defined as

$$\chi = \sqrt{\frac{1}{n}\sum_{i=1}^{n}[I_{\text{exp}}(\varepsilon_i) - I_{\text{sim}}(\varepsilon_i)]^2} + p\sum_{j=1}^{m}[\varepsilon^k_{\max}(j) - \varepsilon^k_{\max}(j+1)]^2. \quad (1)$$

The first term quantifies the goodness of the fit between the measured and simulated spectra. The second term is designed to minimize discontinuities in the potential gradient with depth. The weighting factor p is included to scale the influence of the gradient continuity condition relative to that of the spectral fit. The binding energies are then subjected to incremental random changes and reordering. The process is repeated until χ is minimized. The superscript k in Eq. (1) indicates the order of differences between the values of the peak binding energies. The value $k = 0$ corresponds to the peak binding energies proper, whereas $k = 1$ corresponds to first differences, e.g., $\varepsilon^1_{\max}(j) = \varepsilon_{\max}(j) - \varepsilon_{\max}(j+1)$, and so on. Here $k = 2$ is used. The two terms in Eq. (1) are coupled. That is, increasing parameter p leads to a smoother potential profile but also to a less good fit of the simulated spectrum to experiment. We thus capped p so that the first term does not exceed 0.005 for Si $2p$. The same set of k and p parameters led to the first term being < 0.007 for Ti $2p$.

The asymmetric line shapes for both Ti $2p_{3/2}$ and Si $2p$ angle integrated are well reproduced by our fitting for both $x = 0$ and $x = 0.20$, as seen in Figs. 3(a) and 3(c). For Si $2p$, 350 Si layers were included in the model and the potential was varied in the first 220. The contributions from deeper levels decrease exponentially and we did not observe any improvement in the quality of the Si $2p$ fit for $m \gtrsim 220$. All 31 Ti-containing layers were included and optimized for the $x = 0$ and 0.20 films. The best-fit layer-resolved spectra are shown as contour plots on the left side and the sums over layers are overlaid with the heterojunction spectra on the right side. The fits are excellent in both cases.

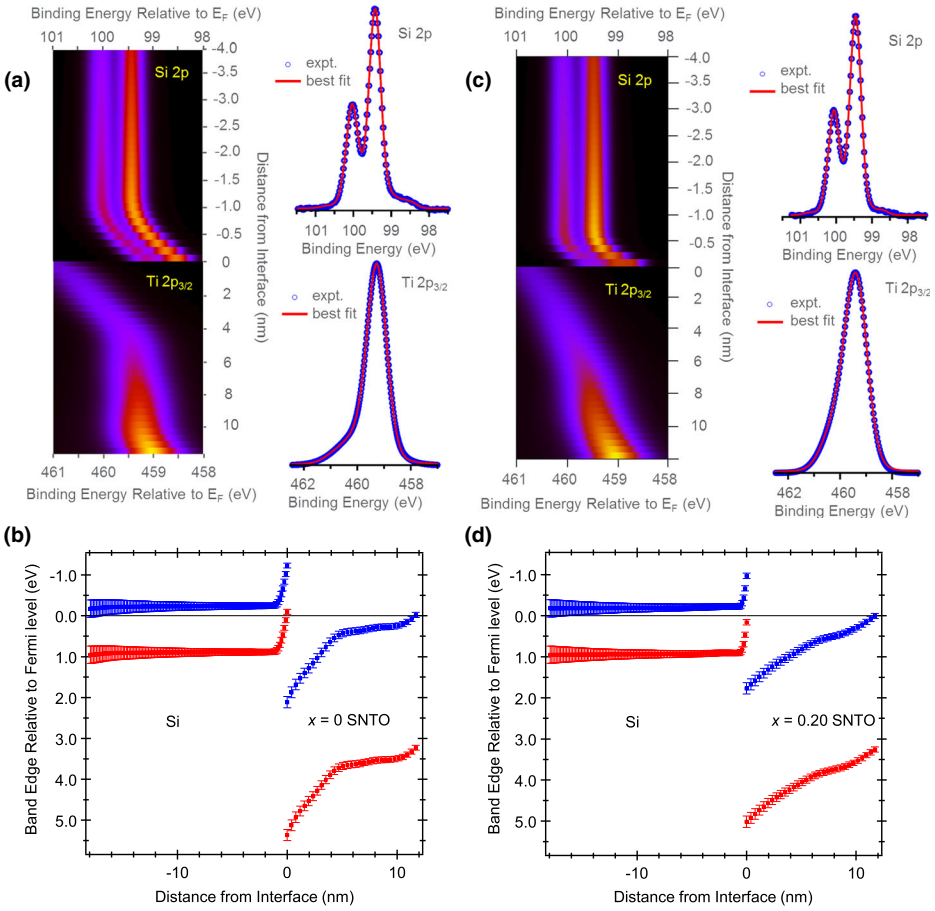

FIG. 3. (a) [(c)] Contour intensity plots of layer-resolved Si $2p$ and Ti $2p_{3/2}$ spectra vs distance from the interface resulting from fitting the spectra from the $x = 0$ ($x = 0.20$) SNTO/Si heterojunction that takes into account built-in fields. Overlays of the sums of all spectra shown in (a) [(c)] to the experimental heterojunction spectra for the $x = 0$ ($x = 0.20$) heterojunction are on the right. (b) [(d)] Band edge profiles for the $x = 0$ ($x = 0.20$) SNTO/Si heterojunction taken from the fits shown in (a) [(c)]. The conduction band-edge profiles are simply the valence band-edge profiles less the band gap for the appropriate material.

This fitting procedure yields a spatial map of the band bending across the $x = 0$ and 0.20 SNTO/Si heterojunctions. In Figs. 3(b) and 3(d) we show the valence (E_V) and conduction (E_C) band-edge energies as a function of distance from the interface, as extracted from the fits shown in Figs. 3(a) and 3(c). For both Si and SNTO, the valence band-edge relative to the Fermi level is given by $E_V(z) = E_{CL}(z) - (E_{CL} - E_V)_{ref}$ (Fig. S10(a)). Here $E_{\mathrm{CL}}(z)$ is the core-level binding energy vs z and $(E_{\mathrm{CL}} - E_V)_{\mathrm{ref}}$ is the energy difference between the same core-level binding energy and the valence band maximum measured for the pure reference material (values given below). The conduction band (CB) edge is given by $E_V(z) - E_g$, where E_g is the band gap. The Si bands bend upward as the interface is approached, terminating with the VBM being very close to the Fermi level at the interface, thereby accommodating a hole gas, consistent with the Hall data. The bands on the SNTO sides of the two heterojunctions also bend upward, moving away from the interface, but with a smaller gradient compared to the Si side. These potential profiles are in excellent agreement with those extracted from angle-resolved HAXPES (Supplemental Material Figs. S5 and S11–S13).

The hole gas and built-in fields arise from the interplay of three phenomena, namely, n-type oxygen impurities in the near-surface region of the Si, a type-III band alignment, and surface depletion in the SNTO. Though nominally undoped, time-of-flight secondary ion-mass spectroscopy (SIMS) reveals heavy oxygen impurity content (up to $\sim 10^{21}$ cm^{-3}) in the near-surface region of the Si wafer, as shown in Supplemental Material Fig. S14 (red). Czochralski-grown Si inherently has oxygen impurities that can diffuse at elevated temperatures and become n-type donors in nominally undoped wafers [25]. Thus, the SNTO/Si heterojunctions are of the isotype variety.

The n-type donors become depleted in the presence of a type-III band arrangement [26], as shown in Figs. 3(b) and 3(d). The valence band offset can be expressed as $\Delta E_V = (\Delta E_{\mathrm{Ti}2p3/2-\mathrm{Si}2p3/2})_{\mathrm{int}} + (E_{\mathrm{Si}2p3/2} - E_V)_{\mathrm{Si}} - (E_{\mathrm{Ti}2p3/2} - E_V)_{\mathrm{SNTO}}$. Here, $(\Delta E_{\mathrm{Ti}2p3/2-\mathrm{Si}2p3/2})_{\mathrm{int}}$ is the difference between

Si $2p_{3/2}$ and Ti $2p_{3/2}$ binding energies directly at the interface, and the second two terms are the differences between core-level binding energies and the VBMs for each reference material, 98.54(4) eV for Si $2p_{3/2}$ in Si(001) and 455.74(4) eV for Ti $2p_{3/2}$ in STO(001). When combined with $(\Delta E_{\mathrm{Ti}2p3/2-\mathrm{Si}2p3/2})_{\mathrm{int}} = 461.13(14) - 98.47(6) = 362.66(15)$ eV, these numbers yield VBM values of 5.46(16) eV for $x = 0$ and 4.86(16) eV for $x = 0.20$. The CB offset (ΔE_C) is given by $\Delta E_V - \Delta E_g = 3.33(16)$ eV for $x = 0$ and 2.74(16) for $x = 0.20$, where ΔE_g is the difference in bulk band gaps for SNTO and Si. Valence band measurements (Supplemental Material Fig. S10) indicate that these SNTO films exhibit the band gap of bulk $SrTiO_3$. This type-III or broken-gap alignment enables electrons in the valence band of Si to transfer to the SNTO conduction band, creating a hole gas in Si.

Fits to the HAXPES spectra also reveal upward band bending near the SNTO surfaces consistent with surface depletion [Figs. 3(b) and 3(d)] [27]. The field induced by surface depletion propagates towards the interface and appears to be coupled to the field associated with the hole gas in Si. If the fields associated with surface depletion and hole gas are coupled, increasing either the thickness or carrier density of the SNTO layer could weaken the coupling, leading to a decrease in n_h. Indeed, transport measurements corroborate this picture, as we find that n_h decreases or disappears with increasing thickness or carrier density of the SNTO layer. Supplemental Material Figs. S15(a) and S15(b) show R_s and R_{xy} data, respectively, for a $x = 0.20$ heterojunction that is 8-nm thicker than the corresponding 12-nm-thick $x = 0.20$ sample considered above [Figs. 1(a) and 1(b)]. The maximum in n_h with temperature becomes nearly $10\times$ smaller with increased thickness, as shown in Supplemental Material Fig. S15(c). Similarly, the hole gas is absent in the $x = 0.60$ heterojunction [Fig. 1(d)], which has the highest carrier density of the SNTO layers.

To quantitatively corroborate the band-edge profiles obtained from our HAXPES analysis, we model potential profiles in SNTO and Si for the $x = 0$ heterojunction based on the information provided by Hall and SIMS (see Supplemental Material [13]). For the $x = 0$ SNTO layer, the band profile and ~ 2 V potential drop determined from HAXPES are consistent with those obtained by self-consistently solving coupled Poisson and Schrödinger equations (Supplemental Material Fig. S16) [28]. Indeed, a high-density electron gas in the SNTO is predicted to arise near the interface, which accounts for the lower valence spectral features we observe (Fig. 2). Hall measurements indicate some of the carriers become localized with lower temperature (Supplemental Material Fig. S17), which gives rise to upturns observed in R_s [Fig. 1(a)]. For Si, the band profile derived from HAXPES matches well with the profile expected from the oxygen impurity distribution obtained from SIMS (Supplemental Material Figs. S18 and S19). Our model thus establishes mutual consistency between three independent experimental techniques.

Owing to the properties of oxides, our SNTO/Si heterojunctions exhibit phenomena not typically observed in conventional semiconductor heterojunctions. The type-III band arrangement *per se* is uncommon. Yet more intriguing, the band arrangement is altered with carrier density, as undoped $SrTiO_3$ on Si exhibits a type-II arrangement [29]. This behavior stems from the ability to significantly alter carrier density or introduce oxygen vacancies, which in turn may affect work functions [30]. Also, we suspect the increase of $\epsilon_{\mathrm{SNTO}}(T)$ with decreasing temperature gives rise to enhanced screening of ionized donors, which has the effect of pushing the n-type carriers of SNTO into the Si, thereby making the formation of the hole gas temperature dependent [27,31]. By understanding how these and other properties of oxides affect charge transfer and built-in fields, novel functional heterojunctions can be realized.

In summary, we report tunable charge transfer, built-in fields, and mapping of the latter via HAXPES in semiconductor-crystalline oxide heterojunctions. We note that techniques of band gap engineering have been adapted to control band alignments at semiconductor-crystalline oxide interfaces [32]. Control of both carrier density, as demonstrated here, and band alignment could enable charge transfer and built-in fields to be engineered across semiconductor-oxide heterojunctions, akin to heterojunctions comprised of III–V semiconductors.

This work was supported by the National Science Foundation (NSF) under Grant No. DMR-1508530. We express our gratitude to Professor J. P. Liu for use of his Dynacool™ system for the cryomagnetic electrical transport measurements. J. H. N. acknowledges helpful conversations with Divine Kumah. XPS measurements and HAXPES fitting performed at Pacific Northwest National Laboratory were supported by the U.S. Department of Energy, Office of Science, Division of Materials Sciences and Engineering under Award No. 10122. The XPS, XRD, and SIMS work was performed in the Environmental Molecular Sciences Laboratory, a national scientific user facility sponsored by the Department of Energy's Office of Biological and Environmental Research and located at PNNL. J. M. L. and A. N. P. gratefully acknowledge funding from the NSF (Grant No. DMR-1350273). This work was performed in part at the Analytical Instrumentation Facility (AIF) at North Carolina State University, which is supported by the State of North Carolina and the NSF (Grant No. ECCS-1542015). The AIF is a member of the North Carolina Research Triangle Nanotechnology Network (RTNN), a site in the National Nanotechnology Coordinated Infrastructure (NNCI). We thank Diamond Light Source for access to beamline I-09 (SI17449-1) that contributed to the results presented here. Additional support was provided by the National Institute of Standards and Technology

(NIST). Certain commercial equipment, instruments, or materials are identified in this document. Such identification does not imply recommendation or endorsement by the National Institute of Standards and Technology, nor does it imply that the products identified are best for that purpose.

[1] S. M. Sze and K. K. Ng, *Physics of Semiconductor Devices* (Wiley-Interscience, Hoboken, NJ, 2006).

[2] D. C. Tsui, H. L. Stormer, and A. C. Gossard, Phys. Rev. Lett. **48**, 1559 (1982).

[3] R. A. McKee, F. J. Walker, and M. F. Chisholm, Phys. Rev. Lett. **81**, 3014 (1998).

[4] R. McKee, F. Walker, and M. Chisholm, Science **293**, 468 (2001).

[5] J. C. Woicik, H. Li, P. Zschack, E. Karapetrova, P. Ryan, C. R. Ashman, and C. S. Hellberg, Phys. Rev. B **73**, 024112 (2006).

[6] C. Rossel, B. Mereu, C. Marchiori, D. Caimi, M. Sousa, A. Guiller, H. Siegwart, R. Germann, J.-P. Locquet, J. Fompeyrine, D. J. Webb, C. Dieker, and J. W. Seo, Appl. Phys. Lett. **89**, 053506 (2006).

[7] M. D. McDaniel, C. Hu, S. Lu, T. Q. Ngo, A. Posadas, A. Jiang, D. J. Smith, E. T. Yu, A. A. Demkov, and J. G. Ekerdt, J. Appl. Phys. **117**, 054101 (2015).

[8] L. Ji, M. D. McDaniel, S. Wang, A. B. Posadas, X. Li, H. Huang, J. C. Lee, A. A. Demkov, A. J. Bard, J. G. Ekerdt, and E. T. Yu, Nat. Nanotechnol. **10**, 84 (2015).

[9] L. Kornblum, D. P. Fenning, J. Faucher, J. Hwang, A. Boni, M. G. Han, M. D. Morales-Acosta, Y. Zhu, E. I. Altman, M. L. Lee, C. H. Ahn, F. J. Walker, and Y. Shao-Horn, Energy Environ. Sci. **10**, 377 (2017).

[10] J. H. Ngai, K. Ahmadi-Majlan, J. Moghadam, M. Chrysler, D. Kumah, F. J. Walker, C. H. Ahn, T. Droubay, Y. Du, S. A. Chambers, M. Bowden, X. Shen, and D. Su, J. Mater. Res. **32**, 249 (2017).

[11] H. P. R. Frederikse and W. R. Hosler, Phys. Rev. **161**, 822 (1967).

[12] J. C. Woicik, *Hard X-ray Photoelectron Spectroscopy (HAXPES)* (Springer International Publishing, Berlin, Germany 2016).

[13] See Supplemental Material at http://link.aps.org/supplemental/10.1103/PhysRevLett.123.026805 for additional information on heterojunction growth and characterization, which includes Refs. [14–19].

[14] X. Sang and J. M. LeBeau, Ultramicroscopy **138**, 28 (2014).

[15] J. L. Campbell and T. Papp, At. Data. Nucl. Data Tables **77**, 1 (2001).

[16] O. Copie, V. Garcia, C. Bodefeld, C. Carretero, M. Bibes, G. Herranz, E. Jacquet, J.-L. Maurice, B. Vinter, S. Fusil, K. Bouzehouane, H. Jaffres, and A. Barthelemy, Phys. Rev. Lett. **102**, 216804 (2009).

[17] E. H. Rhoderick and R. H. Williams, *Metal-Semiconductor Contacts*, (Clarendon Press, Oxford, 1998).

[18] X. Zhang, A. A. Demkov, H. Li, Y. Wei, and J. Kulik, Phys. Rev. B **68**, 125323 (2003).

[19] A. A. Demkov, L. R. C. Fonseca, E. Verret, J. Tomfohr, and O. F. Sankey, Phys. Rev. B **71**, 195306 (2005).

[20] C.-Z. Li, J.-G. Li, L.-X. Wang, L. Zhang, J.-M. Zhang, D. Yu, and Z.-M. Liao, ACS Nano **10**, 6020 (2016).

[21] Y. Du, P. V. Sushko, S. R. Spurgeon, M. E. Bowden, J. M. Ablett, T.-L. Lee, N. F. Quackenbush, J. C. Woicik, and S. A. Chambers, Phys. Rev. Mater. **2**, 094602 (2018).

[22] M. S. J. Marshall, D. T. Newell, D. J. Payne, R. Egdell, and M. R. Castell, Phys. Rev. B **83**, 035410 (2011).

[23] S. Doniach and M. Sunjic, J. Phys. C **3**, 285 (1970).

[24] S. A. Chambers, D. M. Hill, F. Xu, and J. H. Weaver, Phys. Rev. B **35**, 634 (1987).

[25] R. C. Newman, J. Phys. Condens. Matter **12**, R335 (2000).

[26] J. Tersoff, Phys. Rev. B **30**, 4874 (1984).

[27] A. Ohtomo and H. Y. Hwang, Appl. Phys. Lett. **84**, 1716 (2004).

[28] J. H. Ngai, Y. Segal, D. Su, F. J. Walker, S. Ismail-Beigi, K. Le Hur, and C. H. Ahn, Phys. Rev. B **81**, 241307(R) (2010).

[29] S. A. Chambers, Y. Liang, Z. Yu, R. Droopad, and J. Ramdani, J. Vac. Sci. Technol. A **19**, 934 (2001).

[30] Z. Zhong and P. Hansmann, Phys. Rev. B **93**, 235116 (2016).

[31] H.-M. Christen, J. Mannhart, E. J. Williams, and C. Gerber, Phys. Rev. B **49**, 12095 (1994).

[32] J. Moghadam, K. Ahmadi-Majlan, X. Shen, T. Droubay, M. Bowden, M. Chrysler, D. Su, S. A. Chambers, and J. H. Ngai, Adv. Mater. Interfaces **2**, 1400497 (2015).

Correction: A proof request to fix a misspelled word in the third-to-last paragraph in text was not implemented prior to publication and has now been set right.